20. Kroopnick, P. M. The dissolved O_2-CO_2-^{13}C system in the eastern equatorial Pacific. *Deep-Sea Res.* **21,** 211–227 (1974).
21. Charles, C. D. & Fairbanks, R. G. Evidence from Southern Ocean sediments for the effect of North Atlantic deep-water flux on climate. *Nature* **355,** 416–419 (1992).
22. Yu, E.-F., Francois, R. & Bacon, M. P. Similar rates of modern and last-glacial ocean thermohaline circulation inferred from radiochemical data. *Nature* **379,** 689–694 (1996).
23. Adkins, J. F. & Boyle, E. A. Changing atmospheric $\Delta^{14}C$ and the record of deep water paleoventilation ages. *Paleoceanography* **12,** 337–344 (1997).
24. Sikes, E. L. *et al.* Old radiocarbon ages in the southwest Pacific Ocean during the last glacial period and deglaciation. *Nature* **405,** 555–559 (2000).
25. Bard, E. *et al.* The North-Atlantic atmosphere-sea surface ^{14}C gradient during the Younger Dryas climatic event. *Earth Planet. Sci. Lett.* **126,** 275–287 (1994).
26. Toggweiler, J. R. & Samuels, B. in *The Global Carbon Cycle* (ed. Heimann, H.) 333–366 (Springer, Berlin, 1993).
27. Rahmstorf, S. & England, M. H. Influence of southern hemisphere winds on North Atlantic Deep Water flow. *J. Phys. Oceanogr.* **27,** 2040–2054 (1997).
28. Carter, L., Carter, R. M., McCave, I. N. & Gamble, J. Regional sediment recycling in the abyssal S.W. Pacific Ocean. *Geology* **24,** 735–738 (1996).
29. Bianchi, G. G., Hall, I. R. McCave, I. N. & Joseph, L. Measurement of the sortable silt current speed proxy using the Sedigraph 5100 and Coulter Multisizer IIe: precision and accuracy. *Sedimentology* **46,** 1001–1014 (1999).
30. Pardo-Igúzquiza, E., Chica-Olmo, M. & Rodriguez-Tovar, J. CYSTRATI: a computer program for spectral analysis of stratigraphic successions. *Comput. Geosci.* **20,** 511–584 (1994).
31. Mann, M. E. & Lees, J. Robust estimation of background noise and signal detection in climatic time series. *Clim. Change* **33,** 409–445 (1996).
32. Bloomfield, P. *Fourier Analysis of Time Series: an Introduction* (Wiley, London, 1976).

Supplementary information is available on *Nature*'s World-Wide Web site (http://www.nature.com) or as paper copy from the London editorial office of *Nature*.

Acknowledgements

We thank A. Fulop, M. Hall, L. Tiegang, P. Knutz and N. Walsh for experimental assistance, and the captain, crew and shipboard scientific party of Leg 181 for their help. Samples were provided by the Ocean Drilling Program (ODP), with the support of the Natural Environment Research Council and the UK ODP.

Correspondence and requests for materials should be addressed to I.R.H. (e-mail: Hall@cardiff.ac.uk).

Tectonic contraction across Los Angeles after removal of groundwater pumping effects

Gerald W. Bawden*, Wayne Thatcher*, Ross S. Stein*, Ken W. Hudnut† & Gilles Peltzer‡

* *United States Geological Survey, Menlo Park, California 94025, USA*
† *United States Geological Survey, Pasadena, California 91106, USA*
‡ *University of California, Los Angeles, California 90095, USA*

After the 1987 Whittier Narrows[1] and 1994 Northridge[2] earthquakes revealed that blind thrust faults represent a significant threat to metropolitan Los Angeles[3], a network of 250 continuously recording global positioning system (GPS) stations[4,5] was deployed to monitor displacements associated with deep slip on both blind and surface faults. Here we augment this GPS data with interferometric synthetic aperture radar imagery to take into account the deformation associated with groundwater pumping and strike-slip faulting. After removing these non-tectonic signals, we are left with 4.4 mm yr^{-1} of uniaxial contraction across the Los Angeles basin, oriented N 36° E (perpendicular to the major strike-slip faults in the area). This indicates that the contraction is primarily accommodated on thrust faults[6] rather than on the northeast-trending strike–slip faults. We have found that widespread groundwater and oil pumping obscures and in some cases mimics the tectonic signals expected from the blind thrust faults. In the 40-km-long Santa Ana basin, groundwater withdrawal and re-injection produces 12 mm yr^{-1} of long-term subsidence, accompanied by an unprecedented seasonal oscillation of 55 mm in the vertical direction and 7 mm horizontally.

Anthropogenic deformation is evident from a series of 1997–1999 interferograms, which reveal ongoing subsidence of the Wilmington oil field near Long Beach[7], and seasonal uplift and subsidence of the Santa Ana basin, the primary groundwater source for Orange County (Fig. 1). The 5-km-wide Wilmington oil field (W in Fig. 1b) undergoes episodic subsidence (up to 30 mm over 175 days). The 20 km × 40 km Santa Ana basin displays seasonal fluctuations of 50 mm of basin uplift during the late fall through to mid-spring (Fig. 1b and c), and 60 mm of subsidence during the late spring and mid-fall (Fig. 1e and f). The extent of the deformation is similar in each epoch, with the greatest fluctuations near the city of Santa Ana and at the northwestern end of the basin. A profile shows not only that uplift mirrors the subsidence, but also reveals a net annual subsidence of about 16 mm between April 1998 and May 1999) (Fig. 1d).

Sites of likely long-term anthropogenic deformation in metropolitan Los Angeles are revealed by two-year and five-year interferograms (Fig. 2), with subsidence rates up to 34 mm yr^{-1} and uplift rates as high as 9 mm yr^{-1}. Long-term subsidence is seen in the Santa Ana basin (6–13 mm yr^{-1}), the Wilmington (W, 28 mm yr^{-1}) and the Salt Lake (SL, 11 mm yr^{-1}) oil fields. Groundwater pumping near Chino (C)[8] results in a subsidence rate of ~34 mm yr^{-1}. The Santa Fe Springs (SF) and portions of the Baldwin Hills (BH) oil fields are uplifting at 5–9 mm yr^{-1}. Since 1993, fluid injection has exceeded withdrawal in the Baldwin Hills oilfield, consistent with the observed uplift. The uplift mechanism for the Santa Fe Springs oilfield is unclear: the 1984–1999 extraction rates are 9% larger than the injection rates; there is no seasonal component to the uplift; and the uplift rate is much larger than the expected tectonic slip rate[9]. The Newport–Inglewood fault forms a sharp boundary to the deformation (Figs 1 and 2). The range change across the fault seasonally flips sign, indicating that the deformation is associated with groundwater pumping rather than slip along the Newport–Inglewood fault. The groundwater table is presumably truncated against this active fault.

Seasonal water table changes in the Santa Ana basin indicate an association between the aquifer management and surface deformation measured by InSAR[10–12] and GPS (Fig. 3). Wells located near the largest seasonal range change exhibit the greatest seasonal groundwater level fluctuations, whereas wells located elsewhere in the basin have proportionally smaller groundwater elevation and range changes (Fig. 3a). The aquifer is recharged all year round and is pumped during May–September to meet the demand for water in the summer; ~78% of the water pumped from the basin in 1996–1997 came from artificial recharge[13]. On the basis of the geometry of the regional aquifer system[14] and the correlation between the measured surface deformation, groundwater changes and basin

Table 1 Fault model fit to SCIGN GPS data

Faults in model	Nusfit/noise ratio*		Residual contraction†	
	All GPS sites (Fig. 5)	Reliable GPS sites (Fig. 5a)	Azimuth (° east of north)	Rate (mm yr^{-1})
SAF + SJF[6]	5.8	6.4	11 ± 4‡	5.8 ± 1.0‡
This study SAF + SJF	5.3	5.6	20 ± 5	5.1 ± 1.0
All strike–slip faults except PV	3.9	3.9	29 ± 5	4.2 ± 1.0
All strike–slip faults	2.3	1.6	36 ± 5	4.4 ± 0.8

* $M/N = (n^{-1}\Sigma((o-c)/\sigma)^2))^{1/2}$, where M is misfit, N is noise, n is the number of observed GPS velocities o, c is the calculated velocity, and σ is the observed error.
† Contraction azimuth was calculated from the reliable sites in Fig. 5a. Contraction rate is between sites on the Palos Verdes peninsula and sites north of downtown Los Angeles.
‡ Fault model used by ref. 6. They reported a 'north–south' contraction of 5.8 ± 1.9 mm yr^{-1} between the Palos Verdes (PV in Fig. 5a) and San Gabriel Mountains.
The 'all strike-slip fault' model included slip along the San Andreas (SAF), San Jacinto (SJF), Elsinore, Whittier, Newport-Inglewood and Palos Verdes (PV) faults. See Fig. 5 for model description. Uncertainties; 95% confidence reported.
GPS, global positioning system.

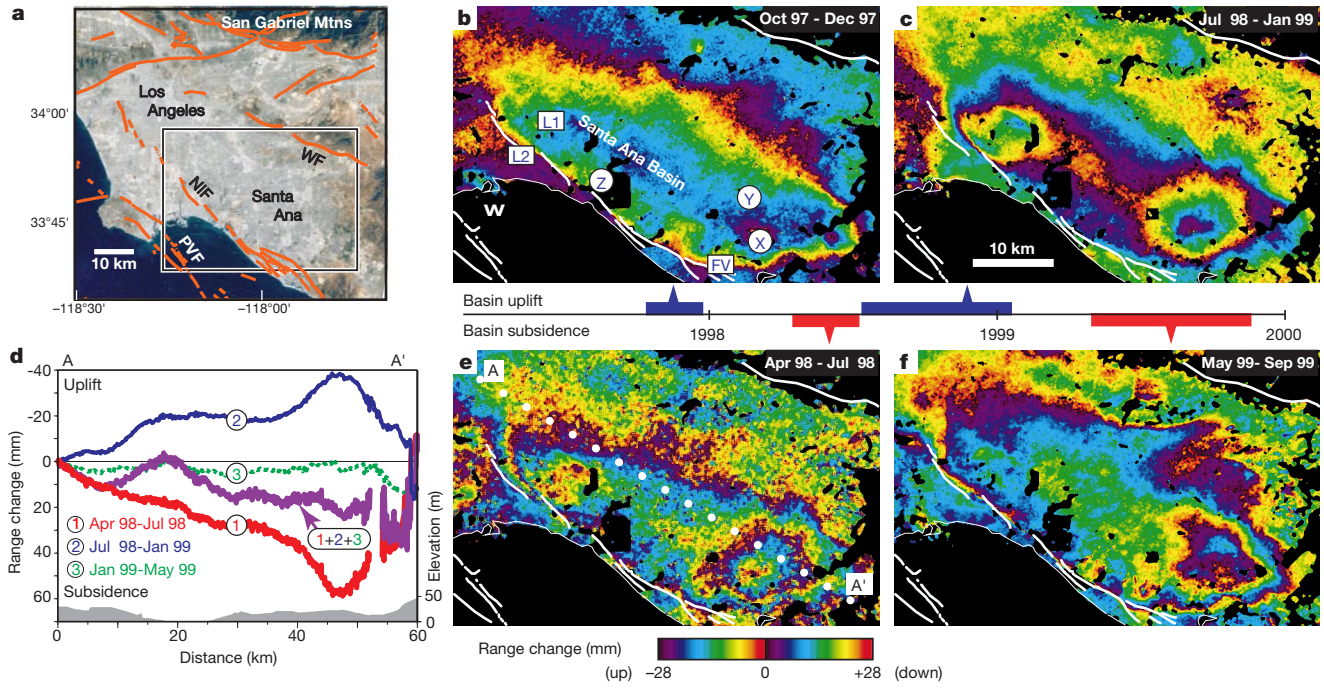

Figure 1 Seasonal deformation in the Santa Ana basin. **a**, Location map for interferograms in **b**, **c**, **e** and **f** (box), and for Figs 2 and 5 (full frame). Faults: PVF, Palos Verdes; NIF, Newport–Inglewood; and WF, Whittier. Differential interferograms (**b**, **c**, **e** and **f**) were constructed by taking the phase difference of paired synthetic aperture radar (SAR) images[17], correcting for the topographic contribution using a United States Geological Survey digital elevation model and for orbital errors by removing a best-fit plane. The interferograms represent line-of-sight range changes between the surface and satellite. One cycle in colours from red through violet represents a decrease in the range of 28 mm between the ground and the satellite. The time history bar in the centre of the figure shows the period that each image spans, and summarizes the type of motion observed in the Santa Ana basin. Blue bar denotes uplift (winter months) and red bar denotes subsidence (summer). **b**, October 1997 to December 1997. This 70-day image shows up to 34 mm of uplift in the Santa Ana basin. W, Wilmington oil field; L1, L2 and FV are GPS sites; and X, Y and Z locate water wells. **c**, July 1998 to January 1999 (175 days). The regions of maximum uplift are at the northwestern and southeastern ends of the basin, with 30 and 50 mm of uplift respectively. **e**, April 1998 to July 1998 (105 days). **f**, May to September 1999 (105 days). The maximum subsidence is 60 mm. Two regions show up to 60-mm subsidence. **d**, Unwrapped range-change profiles along the Santa Ana basin, where unwrapping corrects for phase discontinuities as the phase cycles through increments of 2. Profile location A–A′ is shown as a dotted line in **e**. The deformation is independent of topography, and is thus not an artefact of elevation-dependent atmospheric delays or an inaccurate digital elevation model.

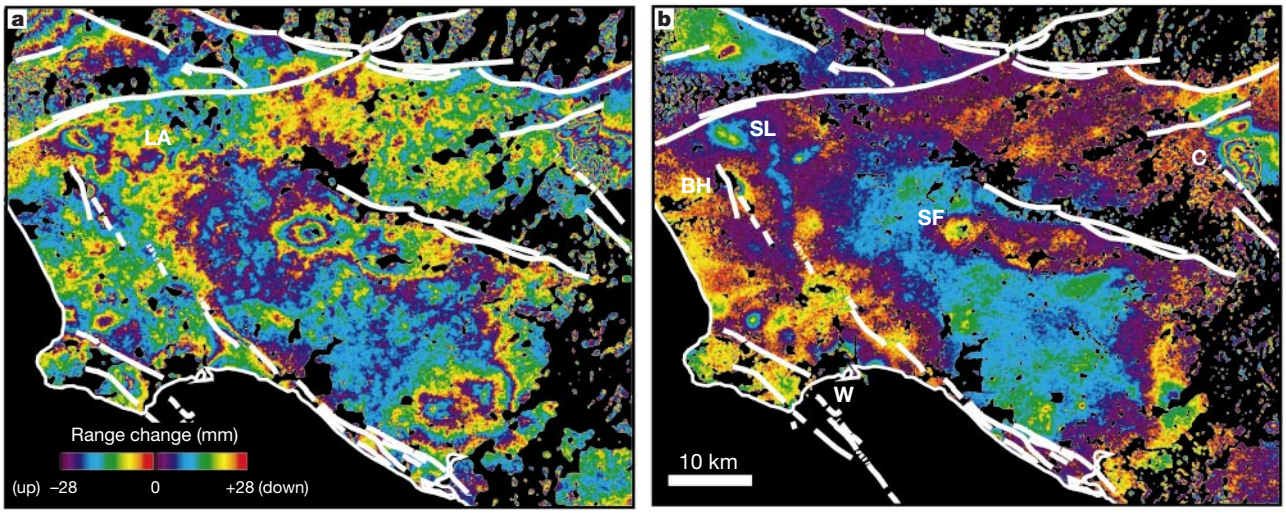

Figure 2 Long-term differential interferograms for metropolitan Los Angeles. **a**, Five-year interferogram between October 1993 and October 1998 shows over 60 mm of subsidence at the southeastern end of the Santa Ana basin during this time period (fringes in the upper left-hand corner are from the uplift associated with the 1994 Northridge earthquake). LA, downtown Los Angeles. **b**, Two-year interferogram between October 1997 and October 1998 shows ~25 mm of subsidence within the basin. BH, Baldwin Hills; C, Chino; LA, Los Angeles; SF, Santa Fe Springs; SL, Salt Lake; and W, Wilmington oil fields. Both **a** and **b** show significant deformation near these labelled sites. The incidence angle of the ERS satellites is 23° from the vertical, thus the interferograms are most sensitive to vertical motion (the unit vector components in the look direction are: north = −0.13, east = 0.37, and up = 0.92). All data are from descending European Space Agency ERS-1 and ERS-2 satellites: track 170, frame 2925.

pumping (Fig. 3), we conclude that the seasonal deformation of the Santa Ana basin results from repeated cycles of groundwater extraction and replenishment. The long-term deformation presumably occurs from unrecoverable inelastic compaction and slow fluid depletion of the less permeable fine-grained sediments within the aquifer, in which the water level drops further after each pumping cycle.

GPS sites on the margin of the Santa Ana basin undergo seasonal horizontal motion toward and away from the basin, while sites within the basin undergo seasonal uplift and subsidence, consistent with a simple elastic model of basin behaviour. The GPS site FVPK, for example, is located on the margin of the basin and is pulled to the northeast (Fig. 3b) when the water table drops (Fig. 3a) and is pushed to the southwest when the water table rises in the winter, producing 14 mm of horizontal and 15 mm of vertical movement. Conversely, the GPS site LBC1 is located within the basin and exhibits little seasonal horizontal movement (±3 mm) but large seasonal vertical motions (±30 mm) (Fig. 3c). Such a pattern, with a high horizontal strain rate gradient near the periphery of an aquifer, also observed elsewhere[15], can be approximated by the response of an elastic material to aquifer pumping or recharge (Fig. 4). Modelled horizontal displacements are largest near the basin margins, where they reach one-third of the subsidence over the aquifer, similar to the ratio observed in the GPS time series. Although the irregular shapes associated with the artificial subsidence and uplift features add local complexities to the horizontal deformation gradient, this elastic model can nevertheless be scaled and used as a template to help understand the observed motions in Figs 1 and 2.

About half of the continuous GPS sites in the Los Angeles basin exhibit superposed effects of tectonic motion and deformation associated with fluid pumping. After removing deformation associated with right-lateral strike–slip faults from the SCIGN velocity field, sites outside the pumping zones show a N 36 ± 5° E contraction across the Los Angeles basin (Fig. 5a, Table 1). GPS sites north of Los Angeles exhibit an average southward velocity of $4.4 \pm 0.8\ \mathrm{mm\,yr^{-1}}$ relative to the Palos Verdes peninsula (PV in Fig. 5a), with no discernible contraction between the Palos Verdes and Catalina Island, 31 km to the south. In contrast, sites that are within or on the periphery of the uplift or subsidence regions have large residual velocities that are generally oriented perpendicular to the local uplift/subsidence gradient (Fig. 5b). Ironically, most of the contaminated sites lie above the Puente Hills, Elysian Park, and Compton blind thrust faults, which limits our ability to infer their geometry (Fig. 5b). Knowing which GPS sites are contaminated by artificial deformation permits either the elimination of these suspect sites or the eventual correction of the artefacts; future SCIGN sites should be placed outside artificial uplift and subsidence regions. Irrespective of the placement of GPS stations, InSAR will

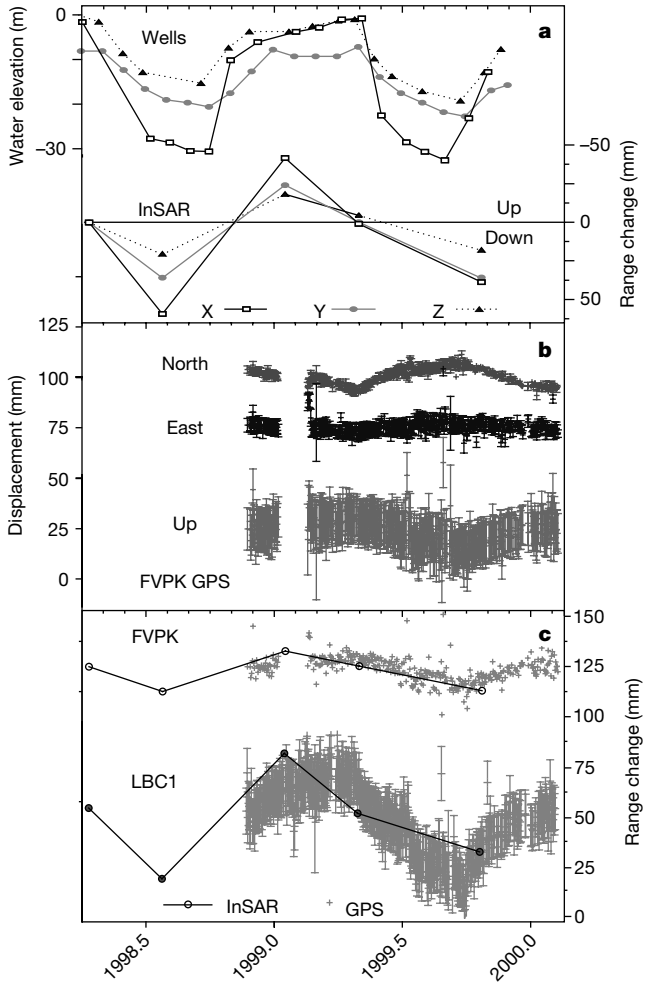

Figure 3 Comparison of groundwater fluctuations, InSAR range change, and detrended GPS time series. **a**, Seasonal elevation changes for three wells located within the Santa Ana basin (top) (located in Fig. 1b) compared with unwrapped InSAR range change time series corresponding to each well location (bottom). For example, the groundwater elevation for Well X drops ~30 m between the winter and summer, corresponding to subsidence of ~100 mm. **b**, The north, east and vertical GPS components for the site FVPK (FV in Fig. 1b). **c**, The three component GPS vector projected onto the InSAR line-of-sight vector at FVPK and LBC1 (L1 in Fig. 1b). An average linear trend has been removed from each horizontal component of the GPS time series. Water table elevations are from the Orange County water district. Well names: X, IRWD-6/1; Y, SA-35/1; and Z, SCWC-LAYT/1.

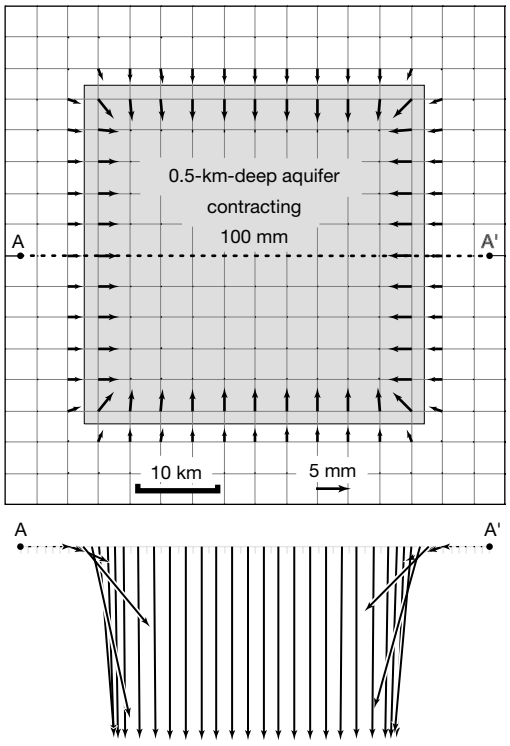

Figure 4 Simulation of basin subsidence. A thin 40 km × 40 km-aquifer is embedded at a depth of 0.5 km in an elastic halfspace with Young's modulus 10^4 MPa and Poisson's ratio 0.25, roughly approximating the Santa Ana basin. Plotted displacements (top, map view; bottom, cross-section A–A′) are for uniform aquifer contraction of 100 mm owing to groundwater extraction; surface displacements would have the opposite sign for aquifer expansion owing to natural recharge or reinjection.

be needed to discriminate between tectonic and non-tectonic signals in the spatially aliased SCIGN array.

Residual GPS velocities that are free of seasonal and anthropogenic effects exhibit nearly uniaxial contraction oriented perpendicular to both the San Andreas and major strike–slip faults. The contraction rate is smaller and rotated 36° clockwise from that determined in ref. 6. This difference arises because, in addition to the San Andreas and San Jacinto faults, we also included interseismic slip on the Palos Verdes, Newport–Inglewood, and Whittier faults to minimize right-lateral GPS displacement gradients (Table 1). Argus *et al.*[6] used a smaller GPS data set to infer that regional contraction across downtown Los Angeles is confined to a 30-km-wide zone between the San Gabriel Mountains and downtown Los Angeles, but we find that the GPS sites needed to resolve the southern boundaries of the contraction region are contaminated (Fig. 5b). No more than half the geodetically observed contraction, or $<2.5–3.5\ \mathrm{mm\ yr^{-1}}$, may be due to thrust faulting[16], with the remainder accommodated by conjugated strike–slip faults in the northern Los Angeles basin. We find not only that the residual contraction is larger than inferred[16], but because the northeast oriented contractional strain rate (56 ± 7 nanostrain $\mathrm{yr^{-1}}$) is eight times larger than the northwest-oriented extension rate and because the contraction is oriented normal to the strike–slip faults (N $36 \pm 5°$ E), the residual contraction cannot be explained by unmodelled strike–slip faulting (Fig. 5a). Instead, the contraction is optimally oriented to accommodate slip on the regional blind and surface-cutting thrust faults. Further densification of the SCIGN net outside the subsidence zones may enable discrimination of competing thrust fault models, which will be vital to seismic hazard assessment in this major urban corridor. □

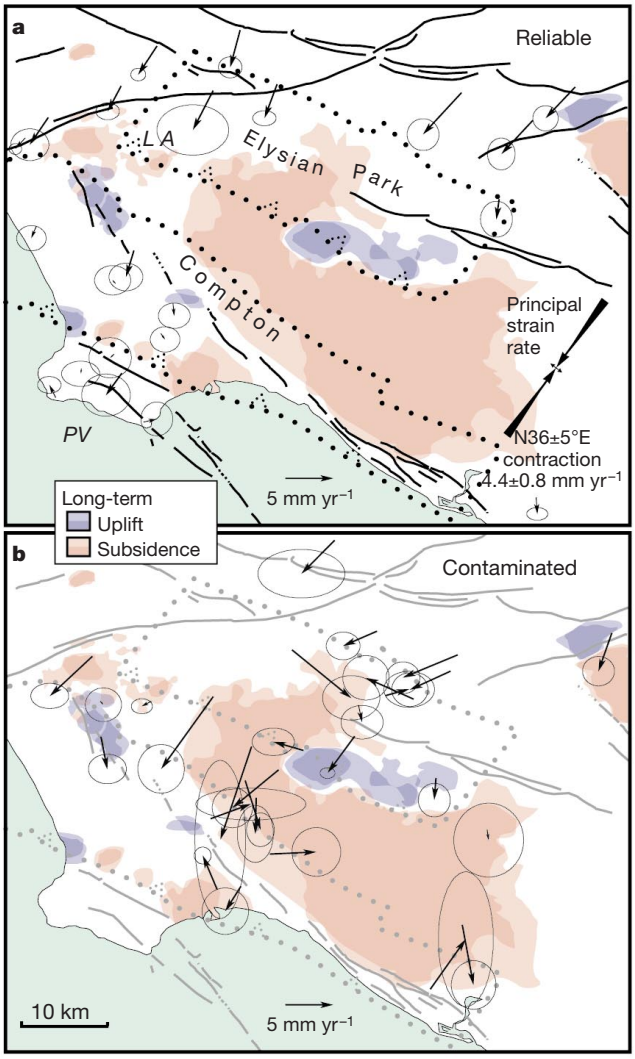

Figure 5 GPS residual velocities after removal of motion associated with strike–slip faults, superimposed on long-term uplift and subsidence features deduced from InSAR. Formal velocity uncertainties were multiplied by 4.5 to account for flicker noise in GPS time series[18]. The displacement field due to the San Andreas, San Jacinto and Elsinore faults was removed from the SCIGN site velocities by using a dislocation in a elastic half-space locked above 20 km depth and slipping below at the estimated Holocene slip rates[19] except for the Mojave segment of the San Andreas fault, where we use 25 mm $\mathrm{yr^{-1}}$ (ref. 6). A 10-km locking depth was used for the Palos Verdes (2.5 mm $\mathrm{yr^{-1}}$), Newport–Inglewood (1.0 mm $\mathrm{yr^{-1}}$), and Whittier (2.5 mm $\mathrm{yr^{-1}}$) faults. Deeper locking depths produced large misfit/noise ratios for the Holocene slip rates[19]. The dotted lines are the surface projections of the Elysian Park and Compton thrust faults (CT)[9,20]. For simplicity, we do not show the segmented Puente Hill thrust fault[9], which lies above the Elysian Park thrust with a more easterly strike. Darker shades are common to both interferograms in Fig. 2. **a**, SCIGN sites outside the margins of the aquifers and oil and gas reservoirs are classified as reliable. **b**, Sites with seasonal variations in their horizontal (≥3 mm $\mathrm{yr^{-1}}$) and vertical (≥8 mm $\mathrm{yr^{-1}}$) time series, or sites located near or within regions of long-term uplift or subsidence.

Received 30 January; accepted 9 July 2001.

1. Hauksson, E. & Jones, L. M. The 1987 Whittier Narrows earthquake sequence in Los Angeles, Southern California; seismological and tectonic analysis. *J. Geophys. Res.* **94,** 9569–9589 (1989).
2. Hauksson, E., Jones, L. M. & Hutton, K. The 1994 Northridge earthquake sequence in California; seismological and tectonic aspects. *J. Geophys. Res.* **100,** 12335–12355 (1995).
3. Dolan, J. F. *et al.* Prospects for larger or more frequent earthquakes in the Los Angeles metropolitan region. *Science* **267,** 199–205 (1995).
4. Prescott, W. H. Satellites and earthquakes: A new continuous GPS array for Los Angeles, yes, it will radically improve seismic risk assessment for Los Angeles. *Eos* **77,** 417 (1996).
5. Bock, Y. *et al.* Southern California Integrated GPS Network (SCIGN)/Permanent GPS Geodetic Array (PGGA). The 1996 SCEC annual report. Report No. 14-08-001-A0899 Vol. 2 (Southern California Earthquake Center, Los Angeles, 1997).
6. Argus, D. F. *et al.* Shortening and thickening of metropolitan Los Angeles measured and inferred by using geodesy. *Geology* **27,** 703–706 (1999).
7. Clarke, D. D., Henderson, C. P. & Strehle, R. Road log to the Long Beach area: Geologic field guide to the Long Beach area. *Ass. Petrol. Geol.* **58,** 135–159 (1987).
8. Ferretti, A., Prati, C. & Roccs, F. Nonlinear subsidence rate estimation using permanent scatters in differential SAR interferometry. *IEEE Trans. Geosci. Remote Sens.* **38,** 2202–2212 (2000).
9. Shaw, J. H. & Shearer, P. M. An elusive blind-thrust fault beneath metropolitan Los Angeles. *Science* **283,** 1516–1518 (1999).
10. Ireland, R. L., Poland, J. F. & Riley, F. S. Land subsidence in the San Joaquin Valley, California, as of 1980. US Geol. Surv. Open-File Rep. 82-370. 134 (US Geol. Survey, Reston, Virginia, 1982).
11. Galloway, D. L. *et al.* Detection of aquifer system compaction and land subsidence using interferometric synthetic aperture radar, Antelope Valley, Mojave Desert, California. *Water Resour.* **34,** 2573–2585 (1998).
12. Galloway, D., Jones, D. R. & Ingebritsen, S. E. Land subsidence in the United States. US Geol. Surv. Circ. 1182. 177 (US Geol. Survey, Reston, Virginia, 1999).
13. Mills, W. *et al.* Orange County Water District, Master Plan Report. 371 (Orange County Water District, Fountain Valley, California, 1999).
14. Poland, J. F. & Piper, A. M. Ground-water geology of the coastal zone, Long Beach–Santa Ana area, California. US Geol. Surv. Water-Supply Paper W1109. 162 (US Geol. Survey, Reston, Virginia, 1956).
15. Carpenter, M. C. Earth-fissure movements associated with fluctuations in ground-water levels near the Picacho Mountains, south-central Arizona, 1980–84 US Geol. Surv. Prof. Paper 497-H. 58 (US Geol. Survey, Reston, Virginia, 1993).
16. Walls, C. *et al.* Escape tectonics in the Los Angeles metropolitan region and implications for seismic risk. *Nature* **394,** 356–360 (1998).
17. Massonnet, D. & Feigl, K. L. Radar interferometry and its application to changes in the Earth's surface. *Rev. Geophys.* **36,** 441–500 (1998).
18. Zhang, J. *et al.* Southern California Permanent GPS Geodetic Array; error analysis of daily position estimates and site velocities. *J. Geophys. Res.* **102,** 18035–18055 (1997).
19. Jackson, D. D. *et al.* Seismic hazards in Southern California; probable earthquakes, 1994 to 2024. *Bull. Seismol. Soc. Am.* **85,** 379–439 (1995).
20. Shaw, J. H. & Suppe, J. Earthquake hazards of active blind-thrust faults under the central Los Angeles Basin, California. *J. Geophys. Res.* **101,** 8623–8642 (1996).

Acknowledgements

This work was supported by NASA Solid Earth and Natural Hazards Program. Water well data was provided by the Orange County Water District. We acknowledge the Southern California Integrated GPS Network and its sponsors, the W. M. Keck Foundation, NASA, NSF, USGS and SCEC, for providing GPS data used in this study. GPS velocity data were provided by SOPAC with assistance from Y. Bock. We thank C. Wicks for his InSAR expertise, R. O. Castle, P. Hseih, J. Langbein, W. Prescott, F. Riley, J. C. Savage, R. Simpson and J. Shaw for reviews, and J. Shaw and A. Plesch for Puente Hills thrust fault data.

Correspondence and requests for materials should be addressed to G.W.B. (e-mail: gbawden@usgs.gov).